Teske, A., Lizarralde, D., Höfig, T.W., and the Expedition 385 Scientists
Proceedings of the International Ocean Discovery Program Volume 385
publications.iodp.org

Data report: petrography of volcaniclastic intervals in IODP Expedition 385 cores from Guaymas Basin, Gulf of California[1]

Priscilla R. Martinez,[2,3] Kathleen M. Marsaglia,[2] and Joann M. Stock[4]

[1] Martinez, P.R., Marsaglia, K.M., and Stock, J.M., 2025. Data report: petrography of volcaniclastic intervals in IODP Expedition 385 cores from Guaymas Basin, Gulf of California. In Teske, A., Lizarralde, D., Höfig, T.W., and the Expedition 385 Scientists, Guaymas Basin Tectonics and Biosphere. Proceedings of the International Ocean Discovery Program, 385: College Station, TX (International Ocean Discovery Program). https://doi.org/10.14379/iodp.proc.385.206.2025
[2] Department of Geological Sciences, California State University Northridge USA. Correspondence author: **priscmartinez@arizona.edu**
[3] Present affiliation: Department of Geosciences, University of Arizona, USA.
[4] Seismological Laboratory, California Institute of Technology, USA.

Contents

Keywords
International Ocean Discovery Program, IODP, *JOIDES Resolution*, Expedition 385, Guaymas Basin Tectonics and Biosphere, Site U1545, Site U1546, Site U1547, Site U1548, Site U1549, Site U1550, volcaniclastic, petrography, volcanism

References (RIS)

MS 385-206
Received 25 November 2023
Accepted 12 October 2024
Published 10 January 2025

Abstract

The Guaymas Basin is a 6 Ma transtensional ocean basin located in the central Gulf of California characterized by active seafloor spreading, off-axis magmatism, and high biogenic and terrigenous sedimentation rates. Sparse volcaniclastic intervals were identified by shipboard scientists in Quaternary sedimentary cores recovered during International Ocean Discovery Program (IODP) Expedition 385. Shipboard visual core descriptions and smear slide analyses were used to identify 57 volcaniclastic intervals, which were then sampled and analyzed macroscopically and microscopically. Petrographic modal analyses were conducted on a subset of 36 thin sections with a total of 300 points counted per thin section. A grain classification scheme was developed from published literature to characterize the compositional and textural variability of volcanic grains in cores from across the basin. Point count percentages reveal that vitric volcanic lithic fragments, particularly brown glass shards, are the dominant clast type observed at all drill sites, whereas crystal-bearing volcanic lithic fragments and mineral grains comprise a minor percentage of the total points counted. The vitric fragments also exhibit a wide range of shard vesicularity and morphologies. This data report presents a petrographic analysis of volcaniclastic deposits recovered during Expedition 385 to elucidate on the modal and spatial distribution of volcanic material in the Guaymas Basin.

1. Introduction

Deep Sea Drilling Project (DSDP) Leg 64, conducted in 1978–1979, was the first major deep-sea drilling effort to target the Guaymas Basin with the objective of investigating the interaction of igneous intrusions and sediments in this rapidly rifting, nascent ocean basin located in the central Gulf of California (Curray, Moore, et al., 1982). The published Leg 64 *Proceedings* volume (Curray, Moore, et al., 1982) contains more than 60 postcruise studies by the Shipboard Scientific Party, including a sedimentologic study by Einsele and Kelts (1982) that better constrained the distribution of turbidites and gravity-flow deposits in the basin. Einsele and Kelts (1982) also proposed that volcanic sand intervals recovered at DSDP Sites 477, 478, and 481 were likely produced by local submarine volcanoes. Petrographic analysis of Leg 64 sand and sandstone samples by Marsaglia (1991) suggests that the basin receives sediment from various sources, including drainage runoff from the Miocene–Pleistocene volcanic terranes on Baja California Sur, Sonora, and Yaqui Rivers from eastern mainland Mexico, and potential volcanic sand and pyroclastic debris from intrabasinal volcanic centers, such as Isla Tortuga.

International Ocean Discovery Program (IODP) Expedition 385 revisited the Guaymas Basin in 2019, recovering 4.2 km of Quaternary sediment and igneous rocks from Sites U1545–U1552 (**Teske et al.**, 2021a; Figure **F1**). Shipboard scientists identified and sampled sparse volcaniclastic intervals (n = 57) in cores from Sites U1545–U1550 (Figure **F2**). A composite summary of macro-

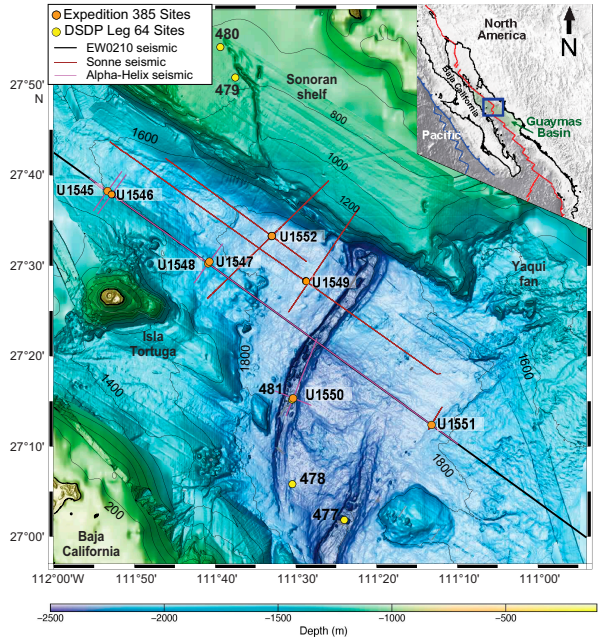

Figure F1. Bathymetric map of Guaymas Basin modified from Teske et al. (2021a), showing Expedition 385 and Leg 64 drill site locations. Inset map shows tectonic setting of Guaymas Basin along Pacific and North American plate boundary in central Gulf of California (green shading), with study location (blue box). Seismic transects conducted prior to Expedition 385 are also shown. Contour lines = 200 m.

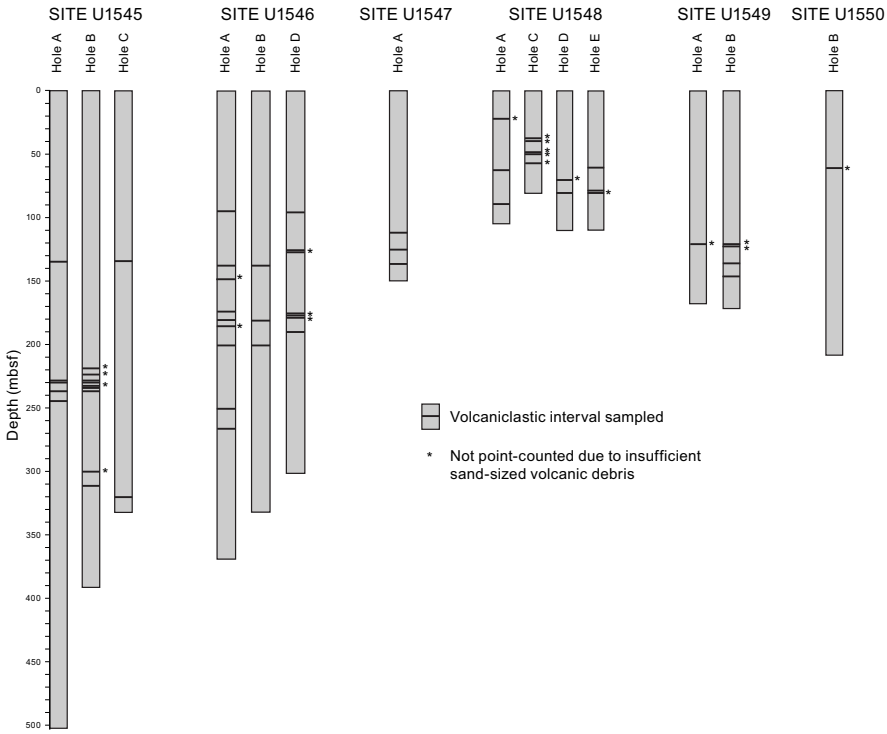

Figure F2. Stratigraphic columns and volcaniclastic interval occurrence, Sites U1545–U1550. Compositional and textural modes were determined for samples with sufficient sand-sized material in this study.

scopic and microscopic analyses for all 57 intervals are detailed in Martinez (2022). A subset of 36 of the 57 samples collected was selected for petrographic analysis in this study based on the abundance and quality of the volcanic material in each sample. The first goal of this project was to create a classification scheme for volcanic particles that depicts 2-D slices of 3-D mafic pyroclasts, hydroclasts, and epiclasts described in published literature. Petrographic analyses revealed that various glass colors, which function as proxies for composition (see discussions in Marsaglia, 1991, 1992, 1993), are found in the basin, including light and dark brown (intermediate to mafic sideromelane), black (mafic tachylite), colorless (silicic pyroclasts), altered, mixed, and orange (palagonite) glass, along with crystal-bearing vitric fragments and trace mineral grains. The vitric particles also exhibit a wide range of glass shard vesicularity and morphologies, including blocky, platy, cuspate, and other distinct fluidal textures. The second goal was to apply the scheme to volcaniclastic intervals recovered during Expedition 385 by conducting point count analyses on a subset of thin sections to document modal percentages of those components. Here, we outline the compositional and textural attributes of volcaniclastic intervals from cores drilled at Expedition 385 sites to provide insights into the downhole variability and spatial distribution of volcanic material in the Guaymas Basin.

2. Methods

Unlithified, silt to sand volcaniclastic intervals were first identified by **Teske et al.** (2021a) in cores from Holes U1545A–U1545C, U1546A, U1546B, U1546D, U1547A, U1548A, U1548C, U1548D, U1548E, U1549A, U1549B, and U1550B (Figure **F3**). A total of 57 intervals were sampled by

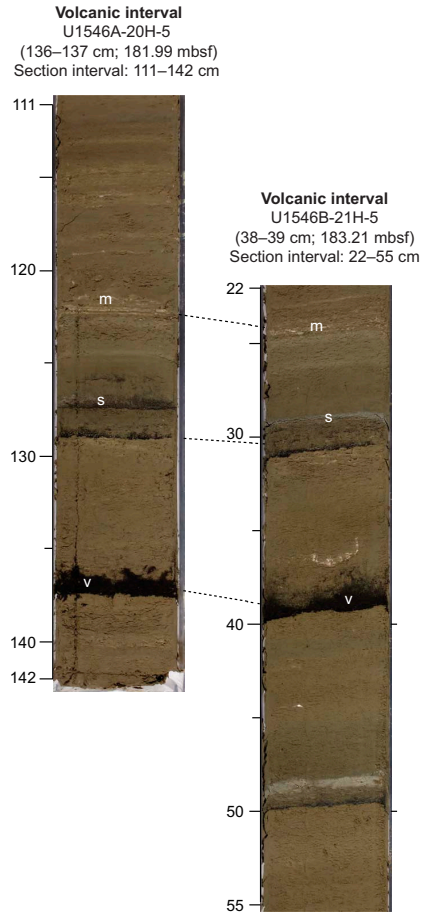

Figure F3. Black volcanic ash (v), gray sand (s), and white micritic laminae (m) correlated by shipboard scientists between Holes U1546A and U1546B. Dashed lines = distinct micritic (top) and ash (middle and bottom) laminae. There are subtle differences in pattern of laminae between holes. White U-shaped feature in Hole U1546B is degraded mollusk fragment. Modified from Teske et al. (2021b).

repository staff from cores stored at the IODP Gulf Coast Repository in College Station, Texas (USA) (Table **T1**). Preliminary smear slide and binocular stereomicroscope observations were made after air drying the samples to identify targets for petrographic analyses. Those targeted samples were then wet sieved to remove the <30 µm fraction and other biosiliceous debris to aid in the concentration of coarser volcanic material using the wet-sieving methods described in Sarna-Wojcicki et al. (2005; Figure **F4**). The wet-sieving procedure involved washing the disaggregated sample through successively finer sieves into plastic beakers, decanting water while retaining settled solids. Each sample was sieved and dried into three fractions: >150 µm for macroscopic analysis, 80–150 µm for petrographic analysis, and 80–30 µm for archival purposes. The <30 µm fraction was not retained, and the procedure did not include the use of any deflocculant or chemical treatment to disaggregate clays from vitric or other mineral particles. Standard thin sections were prepared from sand fractions, primarily the 80–150 µm fractions, and ground to a thickness of 30 µm.

To facilitate volcanic clast identification in thin section, a classification scheme for mafic volcanic particles was developed based on macroscopic (binocular microscope) and microscopic images (scanning electron microscope and photomicrograph) from published studies of mafic epiclastic, pyroclastic, and hydroclastic deposits by Heiken (1972), Fisher and Schmincke (1984), Marsaglia (1993), Clague et al. (2009), Gadley and Marsaglia (2005), and many others (Figure **F5**). The classification scheme was devised specifically to depict 2-D slices as observed in thin section of 3-D mafic particles and expands on the vitric textures outlined by Fisher and Schmincke (1984). Elements of the classification scheme are listed in Table **T2**. Additionally, previous workers (e.g., Marsaglia, 1992, 1993) have broadly linked glass color to composition, and these associations reasonably hold in this study: black (mafic tachylite), brown (mafic to intermediate sideromelane),

Table T1. Sample interval information and summary of analyses conducted for each volcaniclastic sample, Expedition 385. **Download table in CSV format.**

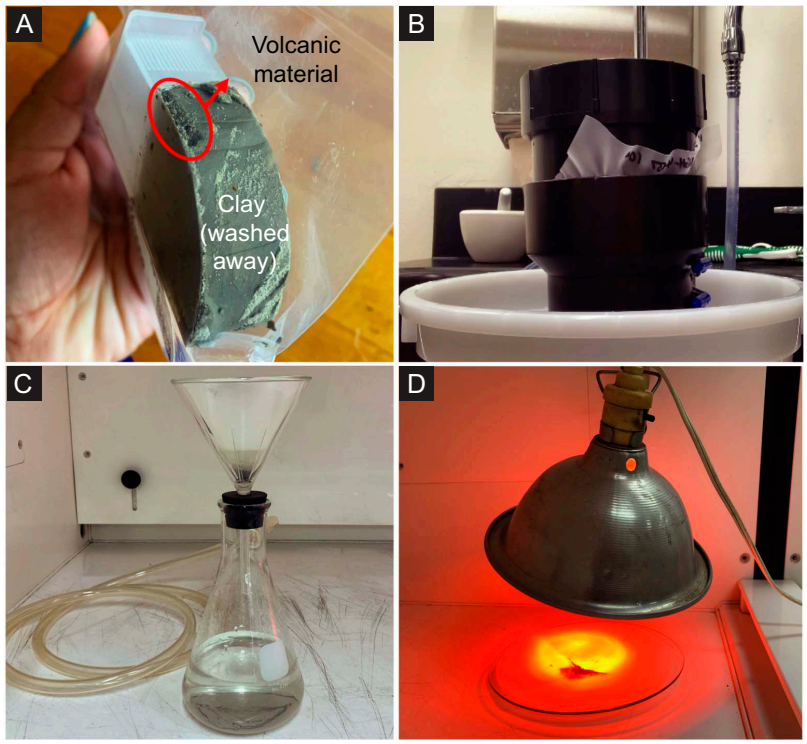

Figure F4. Sample preparation, Sites U1545–U1550. A. Standard Expedition 385 sample bag showing dark volcanic material and surrounding lighter biosiliceous clay; the latter was washed away during processing to isolate glass fraction of sample. B. PVC sieve with nylon sieve and 3000 mL plastic pitcher to retain sample during wet-sieving process. C. Erlenmeyer flask, funnel, and vacuum configuration used to drain water from sample before drying. D. Heat lamp used to dry sample fractions for analyses. Wet-sieving process is based on methods outlined by Sarna-Wojcicki et al. (2005).

Figure F5. Mafic volcanic particle classification scheme combined from various published studies, including photographs and illustrations of 2-D cross sections of volcanic particles in microscopic view. A. Tapered, round-shaped black glass fragments (Pele's tears) modified from Porritt et al. (2012). B. Elongated or stretched brown glass fragments (Pele's hairs) from Alarcon Rise in northern East Pacific Rise modified from Clague et al. (2009). C. Elongate bubble-wall shards (limu o Pele) from Alarcon Rise in northern East Pacific Rise modified from Clague et al. (2009). D. Blocky, dense nonvesiculated glass fragments from pyroclastic and hydroclastic deposits on Lō'ihi Seamount in Hawaii modified from Clague et al. (2003). E. Variations in mafic volcanic lithic fragment glass colors (black and brown) and textures (vitric, microlitic, lathwork, and holocrystalline) in sample of Hawaiian beach sand (plane light) modified from Marsaglia (1993). F, G. Illustrations of crystal-bearing vitric fragments conceptualized from Dickinson (1970). H. Scale of roundness for sedimentary particles modified from Powers (1953). I. Pyroclast classification scheme developed by Gadley and Marsaglia (2005). See Table T2 for abbreviation definitions.

Table T2. Definitions of point count categories and formulas for recalculated parameters, Expedition 385. **Download table in CSV format.**

and colorless (felsic glass or pumice). The classification scheme developed here straddles both epiclastic and pyroclastic realms but with 2-D petrographic description rather than 3-D shape as used in eruption-mode and fragmentation-focused volcanic glass studies (Portner et al., 2015; Dürig et al., 2020b, 2020a); notably, our scheme can be applied to lithified and even diagenetically modified units (e.g., units described by Marsaglia [1991] during Leg 64 within central graben sites). The volcanic lithic fragment (Lv) terminology is commonly used for beach and stream sand on volcanic islands and terrains (e.g., Marsaglia, 1993; Critelli and Ingersoll, 1995; Morrone et al., 2018, 2020) and with cases of lithified volcaniclastics associated with incipient arc magmatism and seamounts (Allen, 2021; Rains et al., 2012; Waldman et al., 2021; Critelli et al., 2002; Marsaglia et al., 1999). The latter are mainly petrologic rather than eruption mode oriented, with volcaniclastic particles of variable origin mixed during littoral to deep marine transport.

Of the 57 sampled intervals, 36 samples were selected for point count analyses based on the abundance and quality of the volcanic material in each sample. To determine compositional and textural modes, a Swift automated stage and point counting system affixed to a Nikon Optiphot petrographic microscope were used to count a total of 300 points on each thin section. Shipboard scientists noted that the mafic silt and sand intervals later sampled for this study included a mix of epiclastic and pyroclastic debris. This debris had been reworked and deposited in the basin (**Teske et al.**, 2021a). We apply the Gazzi-Dickinson method for petrographic analyses (Dickinson, 1970; Ingersoll et al., 1984), which divides volcanic lithic fragments into various compositional and textural types and requires that all sand-sized mineral components in lithic fragments be counted as separate grains. We adopted and modified categories from previous studies of dominantly volcaniclastic intervals that also used this technique (e.g., Hawaii [Marsaglia 1991], Izu-Bonin magmatic arc [Marsaglia, 1992], Circum-Pacific magmatic arcs [Marsaglia and Ingersoll, 1992], and Aeolian magmatic arc [Morrone et al., 2017]). These studies examined epiclastic and pyroclastic debris likely modified by submarine and/or littoral transport and referred to as volcanic lithic debris. The term "lithic" is used in the sedimentologic not volcanological sense. The presence of siliceous and calcareous bioclasts in each sample was noted because they were locally significant, but they were not included in the 300 point total. Several schemes of recalculated parameters (Table **T2**) were then devised to illustrate the compositional and textural variability of the volcaniclastic intervals because of the wide range of grain assemblages observed within the samples. Parameter abbreviations are those of previous petrographic studies (e.g., Marsaglia, 1993; Critelli and Ingersoll, 1995; Morrone et al., 2017, 2018, 2020) that divide the Lv into various subcategories (Table **T2**).

3. Results

Preliminary core image, binocular stereomicroscope, thin section, and smear slide observations used to facilitate point count analyses are detailed in Martinez (2022). The point count categories identified in this study are expanded from those defined by Dickinson (1970) to include glass fragments and mineral grains divided by composition and morphology (i.e., degree of vesicularity), along with their associated definitions and recalculated parameters (Table **T2**). Figure **F6** consists of photomicrographs of select common grain types observed in thin section and assigned as point count categories for petrographic analysis. The point count data for 36 thin sections produced from this analysis are found in Table **T3**. The proportions of vitric composition categories calculated from the bulk vitric point count population (lithic volcanic with vitric texture [Lvv]) for each sample are listed in Table **T4**. Compositional and textural variability at Sites U1545–U1549 are displayed in ternary plots in Figures **F7**, **F8**, **F9**, **F10**, and **F11** that were constructed using recalculated parameters of raw point count data shown in Table **T5**. The raw point count data are expressed as bulk percentages in Table **T6** to demonstrate distributions and trends for vitric fragment compositions within and among sites, as illustrated in Figures **F12**, **F13**, **F14**, **F15**, **F16**, **F17**, **F18**, and **F19**.

3.1. Compositional modes

The point count data for the 36 samples counted (10,800 total grains) indicate that vitric volcanic lithic fragments comprise an average of 91.2% of the total composition of these intervals, and crystal-

bearing volcanic lithic fragments and mineral grains comprise an average of 5.02% and 3.76%, respectively (Table **T5**; Figure **F7**).

The volcanic lithic fragments (Lvv) mentioned above can be further divided as follows: light brown (70.2%), nontranslucent altered (17.2%), colorless (5.2%), black (3.7%), mixed brown/black (2.2%), dark brown (1.1%), and orange (0.4%) glass (Table **T4**). The prevalence of brown and black colors suggests a predominant intermediate to mafic composition signature within the vitric component point count population. Brown, colorless, and orange glass fragments appear mostly translucent in transmitted light, with dark brown glass having a slightly lower translucency than all other glass types (Figure **F6**). In transmitted light, black glass fragments are opaque and commonly contain plagioclase microlites and laths surrounded by fine opaque minerals, referred to as tachylite. In contrast, the colorless vitric fragments are translucent and lack crystals. Figure **F8** illustrates the distribution of brown (light and dark), black, and colorless glass in the sample suite, highlighting the high abundance of brown glass across all sites, except for two samples from Holes U1545B and U1546A, which primarily consist of colorless glass. Altered glass colors vary from reddish brown to dark gray to black and are likely products of intermediate to mafic glass (Figure **F6G**). The vitric fragments referred to as "mixed" glass appear to be composed of a combination of light brown and black glass, but it is unknown if this component represents a distinct type of alteration or if it is an

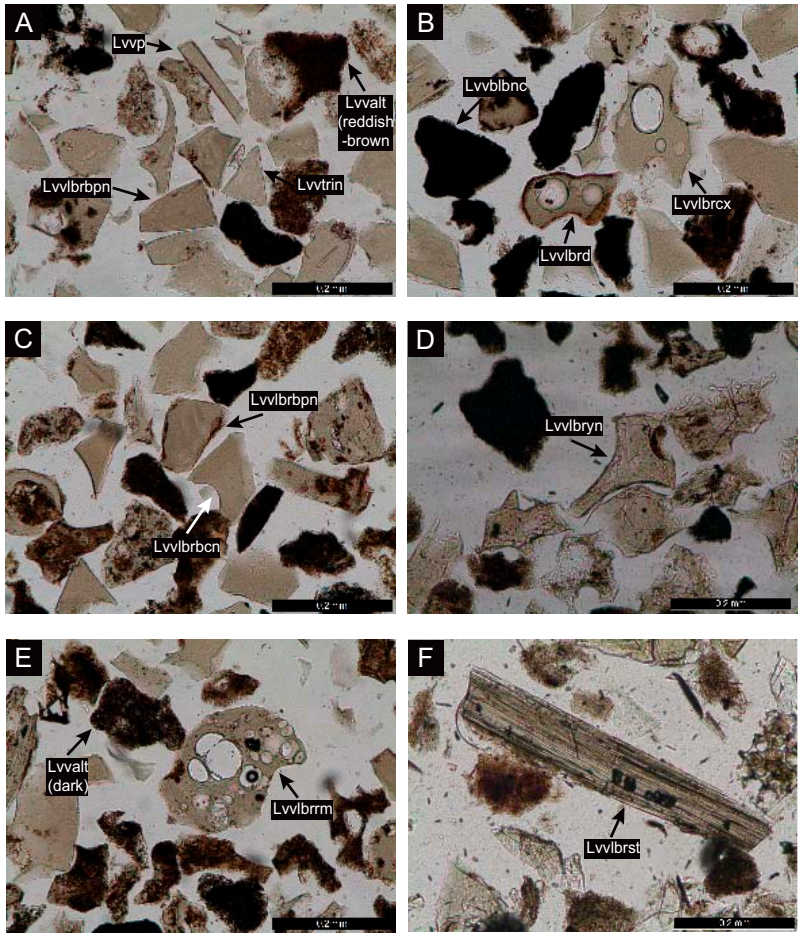

Figure F6. Volcaniclastic deposits highlighting select point count categories. See Table T2 for abbreviation definitions. A. Various light brown glass morphologies, such as platy (Lvvp), blocky, nonvesicular planar (Lvvlbrbpn), and triangle-shaped shards (Lvvtrin), along with reddish brown altered glass (Lvvalt) (385-U1546B-21H-7, 38–39 cm; 183.21 mbsf). B. Light brown dumbbell-shaped (Lvvlbrd), complex cuspate glass (Lvvlbrcx), and black blocky (Lvvblbnc) glass (385-U1547A-27X-2, 19–23 cm; 136.78 mbsf). C. Blocky light brown shard with single curved edge (Lvvlbrbcn) and planar edges (Lvvlbrbpn) (385-U1545C-15H-6, 31–33 cm; 134.53 mbsf. D. Light brown cuspate, Y-shaped (Lvvlbryn) glass (385-U1545A-15H-9, 44–47 cm; 135.18 mbsf). E. Dark-colored altered (Lvvalt) and light brown, round-shaped glass (Lvvlbrrm) with interval vesicles (385-U1545C-15H-6, 31–33 cm; 134.53 mbsf). F. Light brown stretched glass (Lvvlbrst) (385-U1545A-41F-1, 46–48 cm; 244.86 mbsf). Note biogenic particle to right of light brown stretched glass. (Continued on next page.)

actual mix of two glass types that formed contemporaneously (Figure **F6H**). Orange glass shards are rarely observed throughout each site but are characteristically translucent in transmitted light and likely palagonitic in composition (Figure **F6J**).

Crystal-bearing volcanic fragments exhibit vitric groundmasses that span all color varieties and contain microlites (<63 μm; lithic volcanic fragment with microlitic texture [Lvml]) or laths (>63

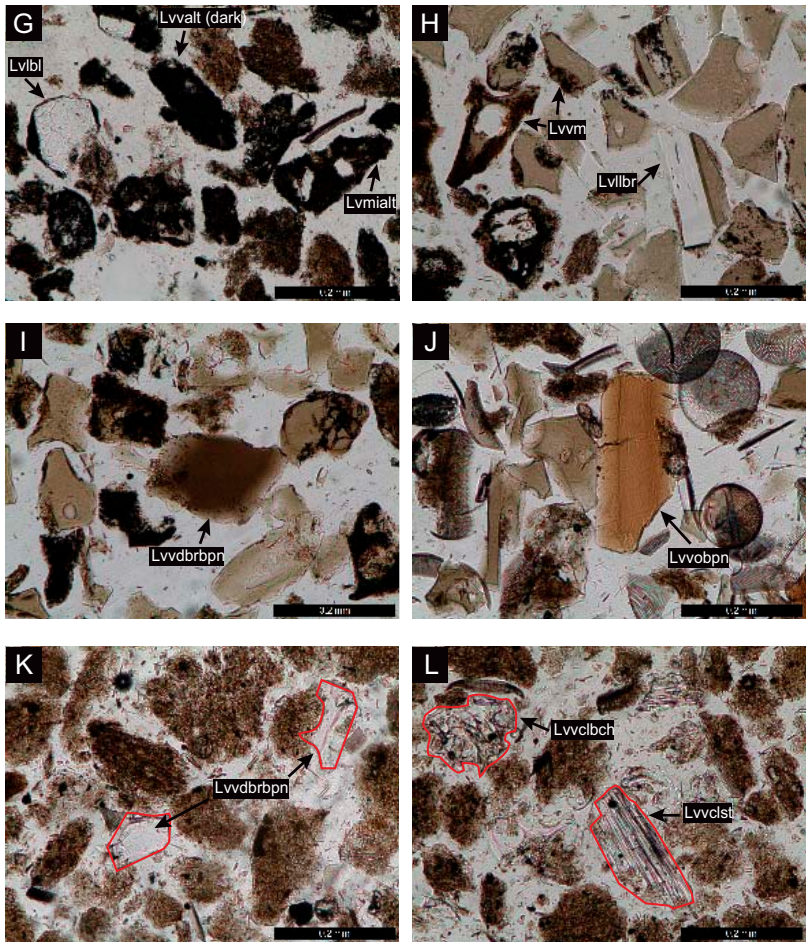

Figure F6 (continued). G. Black glass with plagioclase lath (Lvlbl), along with dark-colored altered glass (Lvvalt) with microlites (Lvmialt) (385-U1546A-40F-1, 130–131 cm; 251 mbsf). H. Light brown glass with plagioclase lath (Lvllbr) and mixed glass (Lvvm) (385-U1546B-21H-7, 38–39 cm; 183.21 mbsf). I. Blocky dark brown glass (Lvvdbrbpn) (385-U1545C-15H-6, 31–33 cm; 134.53 mbsf). J. Blocky orange glass shard (Lvvobpn), along with various light brown glass fragments, diatoms, and spicules (385-U1546B-17H-1, 80–84 cm; 137.5 mbsf). K, L. Colorless glass with blocky nonvesicular (Lvvclbcn), highly vesicular (Lvvclbch), and stretched (Lvvclst) morphologies (385-U1546A-44F-2, 84–86 cm; 265.4 mbsf). Colorless glass is outlined in red. Other patchy brown pseudograins surrounding colorless glass fragments are agglomerations of semilithified biosiliceous matrix created during sample processing.

Table T3. Raw point count data for samples, Sites U1545–U1549. **Download table in CSV format.**

Table T4. Proportions of each vitric composition for 37 samples point counted in this study, Sites U1545–U1549. **Download table in CSV format.**

Table T5. Recalculated parameter data, Sites U1545–U1549. **Download table in CSV format.**

Table T6. Bulk percentages calculated from raw point count data for general categories in Table T5, Sites U1545–U1549. **Download table in CSV format.**

μm; lithic volcanic fragment with lathwork texture [Lvl]) of plagioclase (Figure **F6G, F6H**). On average, lithic volcanic fragments with crystalline textures range from microlitic (2.1%) and lathwork (2.6%) fragments to polymineralic (holocrystalline) grains (0.35%). The monomineralic grains identified in the samples comprise a relatively small percentage (3.8%) of the total composition. Plagioclase is the dominant monocrystalline component, ranging as high as 13% of one sample's total composition (Sample 385-U1548E-7H-2, 102–104 cm, top depth at 60.22 m below seafloor [mbsf] in Table **T6**) but averaging <1% of the total point counted population. Sand-sized plagioclase crystals in lathwork fragments were counted as individual components but observed in trace amounts (<0.01%). Trace amounts of pyroxene, altered biotite, and undifferentiated opaque minerals are also present.

3.2. Textural modes

The glassy fragments identified in this study were classified according to their degree of vesicularity and morphology. To evaluate the degree of glass vesicularity, a classification scheme for shard vesicularity developed by Gadley and Marsaglia (2005) was used, which ranges from nonvesicular

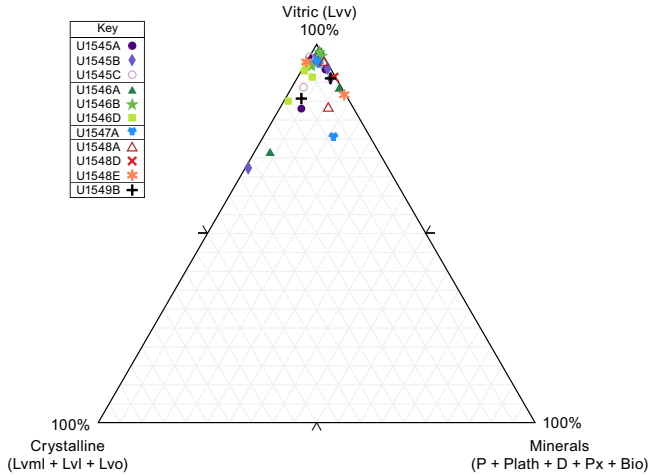

Figure F7. Ternary Plot 1, Sites U1545–U1549. Total vitric (Lvv) vs. total crystal-bearing volcanic fragments (crystalline; Lvmi + Lvl + Lvo) vs. total minerals (P + Plath + D + Px + Bio). Ternary parameters are defined in Table T2 and percentages are listed by sample in Table T4. Tick marks on outer perimeter of ternary plot denote 50th percentile compositional or textural intervals. See Table T2 for abbreviation definitions.

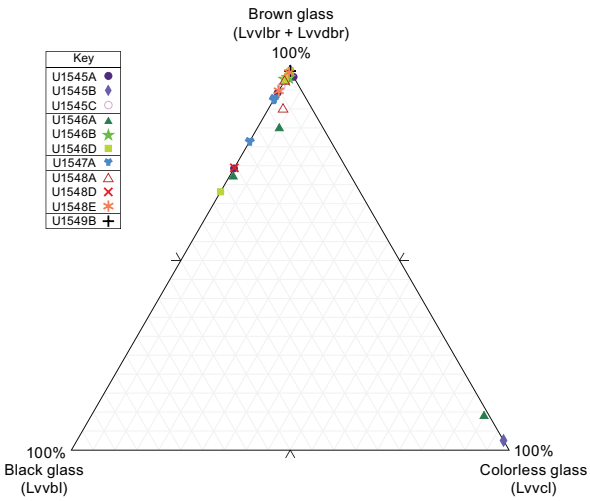

Figure F8. Ternary Plot 2, Sites U1545–U1549. Total brown glass (Lvvlbr + Lvvdbr) vs. total black glass (Lvvbl) vs. total colorless glass (Lvvcl). Ternary parameters are defined in Table T2 and percentages are listed by sample in Table T4. Tick marks on outer perimeter of ternary plot denote 50th percentile compositional or textural intervals.

to highly vesicular (Figure **F5I**). The various glass shard morphologies observed in thin section and their associated definitions are described in Table **T3** and discussed further below.

Light brown glass, the most abundant type of vitric volcanic fragment, exhibits the widest range of shard vesicularity (Figure **F9**) and morphology (Figures **F10**, **F11**), including blocky (equant shards with both curved and planar edges), platy (elongated strands that appear to be the broken walls of large, isolated bubbles), cuspate (Y-shaped), triangle-shaped, and stretched (strands or fragments with ribbed surfaces formed by elongate vesicles) textures. Other less prominent but

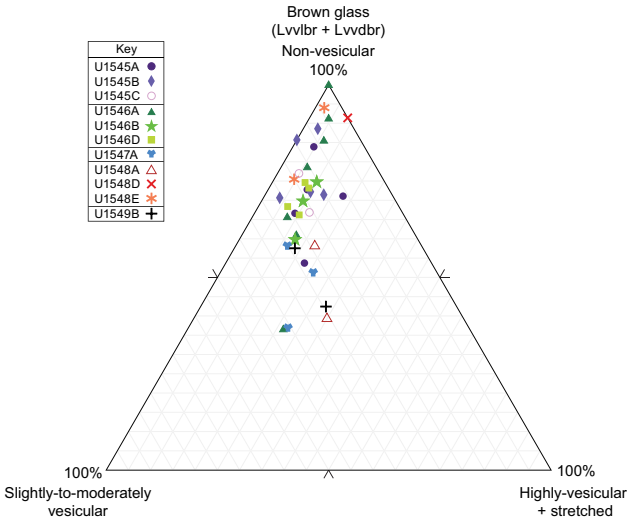

Figure F9. Ternary Plot 3, Sites U1545–U1549. Brown (Lvvlbr + Lvvdbr) nonvesicular (Lvvlbryn + Lvvlbrtrin + Lvvlbrrn + Lvvlbrp + Lvvlbrbcn + Lvvlbrbpn + Lvvdbrbcn) vs. brown slightly to moderately vesicular (Lvvlbrys + Lvvlbrtris + Lvvlbrrs + Lvvlbrrm + Lvvlbrd + Lvvlbrbsc + Lvvlbrbmc Lvvlbrbsp + Lvvlbrbmp + Lvvdbrbnc + Lvvdbrbsc + Lvvdbrbmc) vs. brown highly vesicular to stretched (Lvvlbrcx + Lvvlbrbhc + Lvvlbrst + Lvvdbrst) glass. Ternary parameters are defined in Table T2 and percentages are listed by sample in Table T4. Tick marks on outer perimeter of ternary plot denote 50th percentile compositional or textural intervals. See Table T2 for abbreviation definitions.

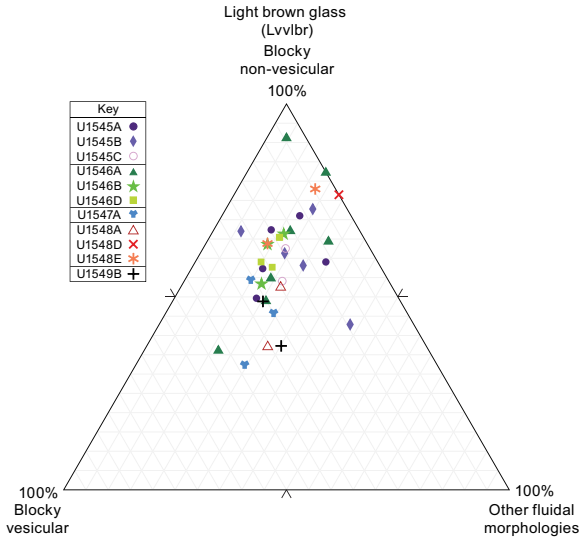

Figure F10. Ternary Plot 4, Sites U1545–U1549. Light brown blocky nonvesicular glass (Lvvlbrbcn + Lvvlbrbpn) vs. light brown blocky vesicular glass (Lvvlbrbsc + Lvvlbrbmc + Lvvlbrbhc + Lvvlbrbsp + Lvvlbrbmp) vs. other light brown (Lvvlbrcx + Lvvlbryn + Lvvlbrys + Lvvlbrtrin + Lvvlbrtris + Lvvlbrrn + Lvvlbrrs + Lvvlbrrm + Lvvlbrp + Lvvlbrd + Lvvlbrst) glass with fluidal morphologies totaled for all samples at Sites U1545–U1549. Ternary parameters are defined in Table T2 and percentages are listed by sample in Table T4. Tick marks on outer perimeter of ternary plot denote 50th percentile compositional or textural intervals. See Table T2 for abbreviation definitions.

notable morphological categories include round-shaped, dumbbell-shaped, and complex bubble-wall textures (Figure **F6B, F6E**). Round-shaped brown glass fragments have drop-like morphologies with smooth outer surfaces rarely disrupted by internal vesicles and dumbbell-shaped glass fragments have an hourglass shape with round edges and internal vesicles (Figure **F6E**).

Dark brown glass fragments are largely nonvesicular-to-moderately vesicular blocky shards with the exception of occasional stretched glass shards (Figure **F6F**). Similarly, black glass fragments are largely blocky or irregularly shaped with vesicularity ranging from nonvesicular to highly vesicular. Trace amounts of round-shaped tachylite fragments were found in only one sample (385-U1547A-27X-2, 19–23 cm, top depth at 136.78 mbsf in Table **T6**). However, most tachylitic fragments have a rounded appearance that differs from the round-shaped morphology primarily observed in brown glass fragments (Figure **F6E**) due to the irregularity in the grain's overall shape, which may reflect transport prior to deposition. Mixed brown–black glass and orange glass fragments are predominantly blocky nonvesicular shards with minor amounts of slightly to moderately vesicular blocky shards. Colorless glass shards exhibit exclusively nonvesicular to highly vesicular blocky or stretched ("woody") pumice textures. Fragments of altered glass exhibit morphologies ranging from blocky to stretched (woody) scoria, although other undifferentiated altered fragments were also identified as having irregular, nonequant shapes, similar to those observed in black tachylitic glass.

3.3. Downhole compositional trends within and among sites

Light brown (Figure **F12**) and altered (Figure **F13**) vitric component percentages are consistently high downhole at all sites, with light brown blocky glass shards being the dominant component, except for a few deeper samples that are rich in colorless glass at 313 and 265 mbsf in Holes U1545B and U1546A, respectively (Figure **F14**). Site U1549 is located at a greater depth below sea level within the basin and shows limited downhole patterns because of the few data points counted. However, the percentage of light brown glass is consistently higher than any other component throughout Hole U1549B (Figure **F12**). Percentages of dark brown (Figure **F15**), black (Figure **F16**), mixed (Figure **F17**), and orange (Figure **F18**) glass fragments are relatively low at all sites and overall decrease in abundance with depth. The abundances of crystal-bearing vitric fragments and minerals are also relatively minor throughout each hole. The sporadic distribution of micro- to holocrystalline volcanic fragments in the analyzed samples is shown in Figure **F19**. It is important to note that despite their proximity (Figure **F1**), extensive variability exists between Sites

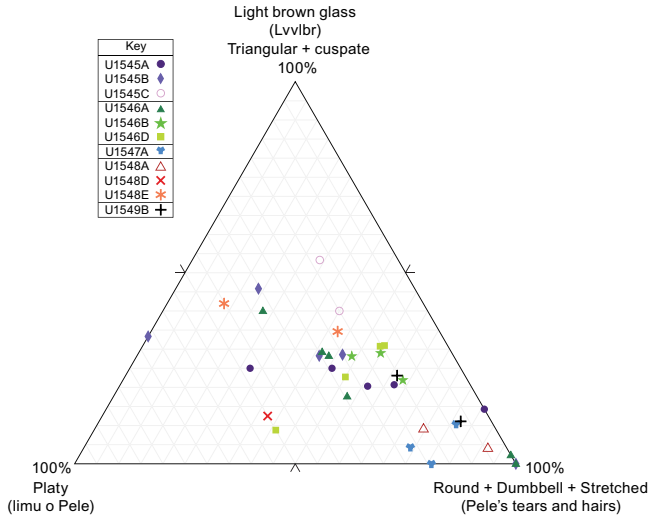

Figure F11. Ternary Plot 5, Sites U1545–U1549. Light brown triangular- and cuspate-shaped (Lvvlbrtrin + Lvvlbrtris + Lvvlbryn + Lvvlbrys) vs. platy (Lvvlbrp) vs. round-shaped + dumbbell-shaped + stretched (Lvvlbrrn + Lvvlbrrs + Lvvlbrrm + Lvvlbrd + Lvvlbrst) glass. Ternary parameters are defined in Table T2 and percentages are listed by sample in Table T4. Tick marks on outer perimeter of ternary plot denote 50th percentile compositional or textural intervals. See Table T2 for abbreviation definitions.

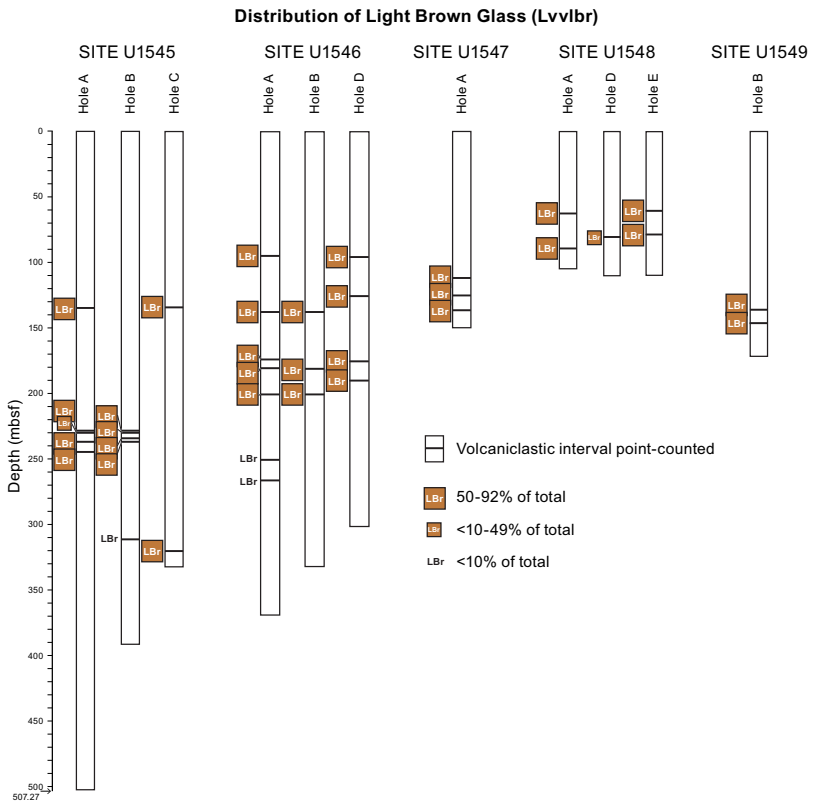

Figure F12. Total percent of light brown glass (Lvvlbr) in samples from each site showing the distribution of this component in site stratigraphy across the basin. Percentages taken from Table T6 based on data presented in Table T3.

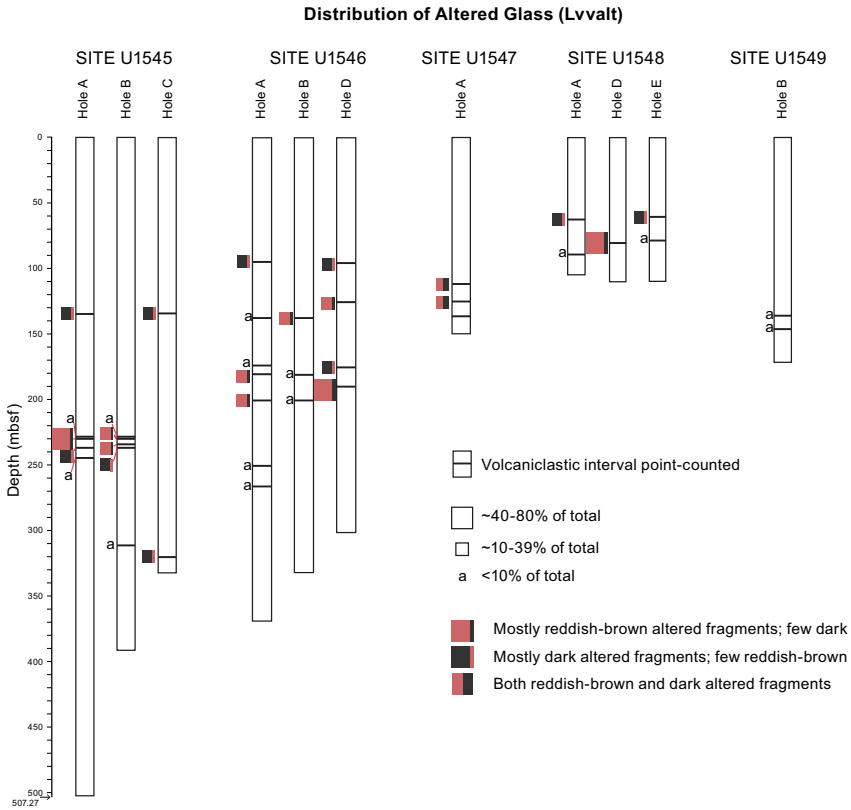

Figure F13. Total percent of altered glass (Lvvalt) in samples from each site showing distribution of this component in site stratigraphy across basin, Sites U1545–U1549. Percentages taken from Table T6 based on data presented in Table T3.

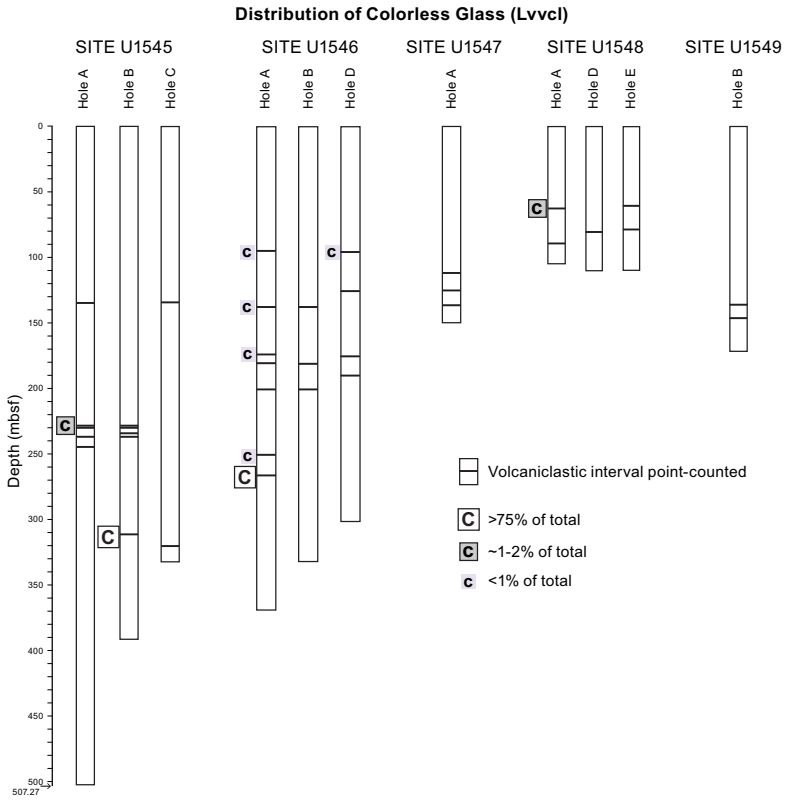

Figure F14. Total percent of colorless glass (Lvvcl) in samples from each site showing distribution of this component in site stratigraphy across basin, Sites U1545–U1549. Percentages taken from Table T6 based on data presented in Table T3.

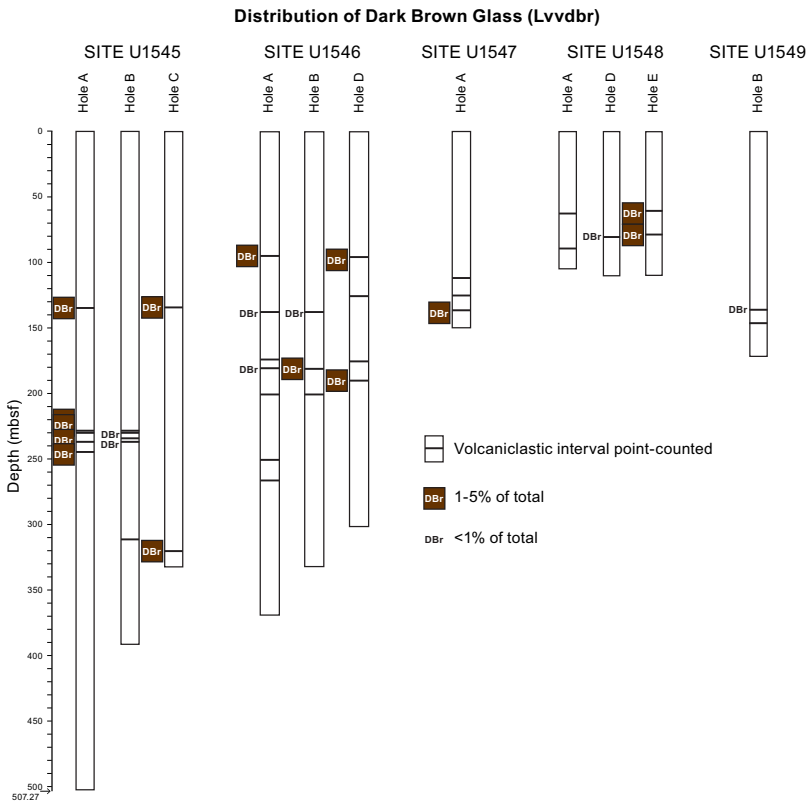

Figure F15. Total percent of dark brown glass (Lvvdbr) in samples from each site showing distribution of this component in site stratigraphy across basin, Sites U1545–U1549. Percentages taken from Table T6 based on data presented in Table T3.

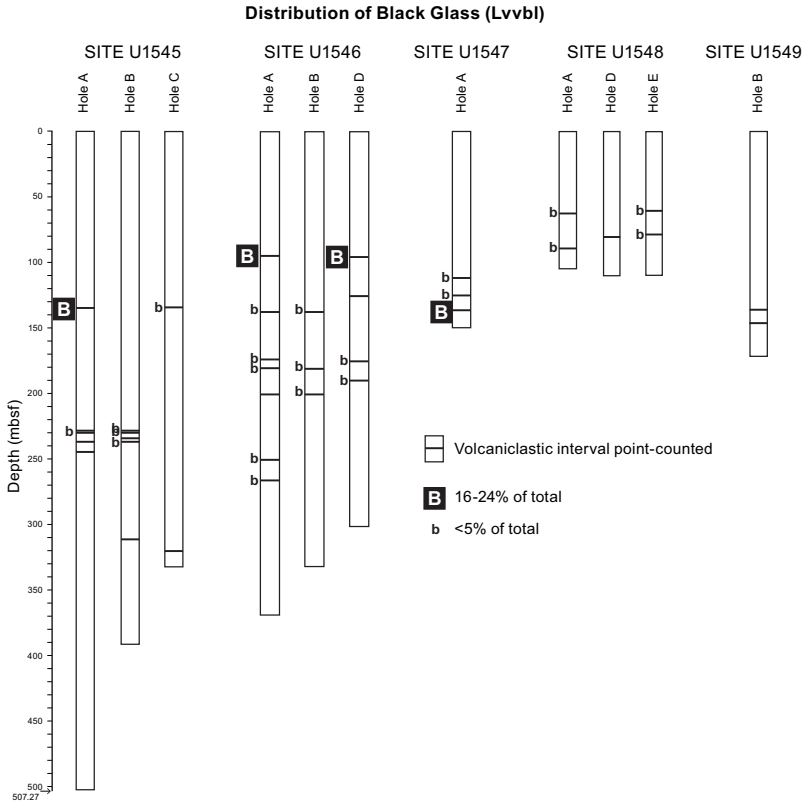

Figure F16. Total percent of black glass (Lvvbl) in samples from each site showing distribution of this component in site stratigraphy across basin, Sites U1545–U1549. Percentages taken from Table T6 based on data presented in Table T3.

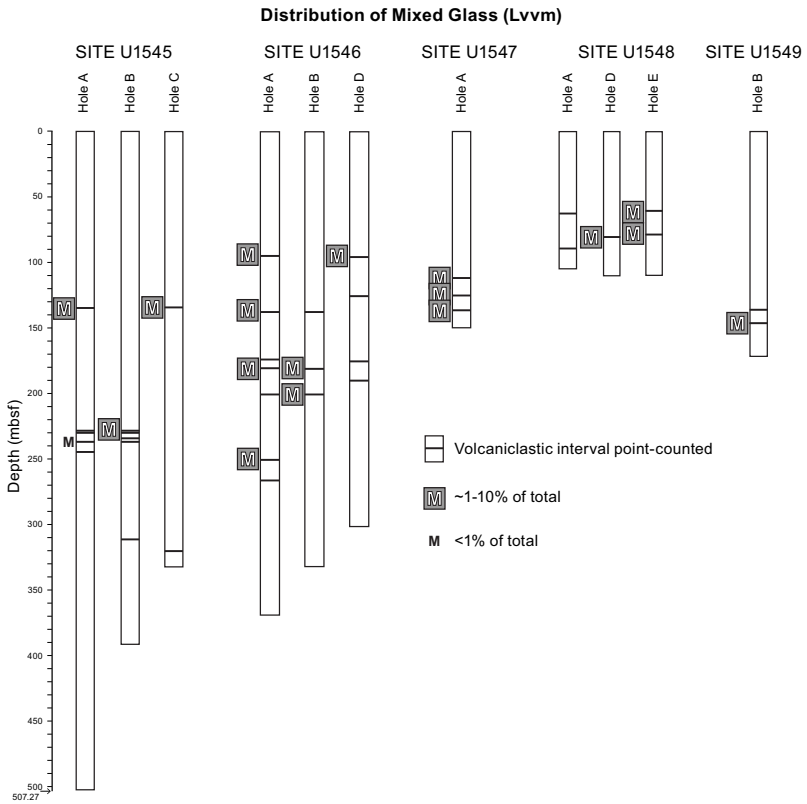

Figure F17. Total percent of mixed glass (Lvvm) in samples from each site showing distribution of this component in site stratigraphy across basin, Sites U1545–U1549. Percentages taken from Table T6 based on data presented in Table T3.

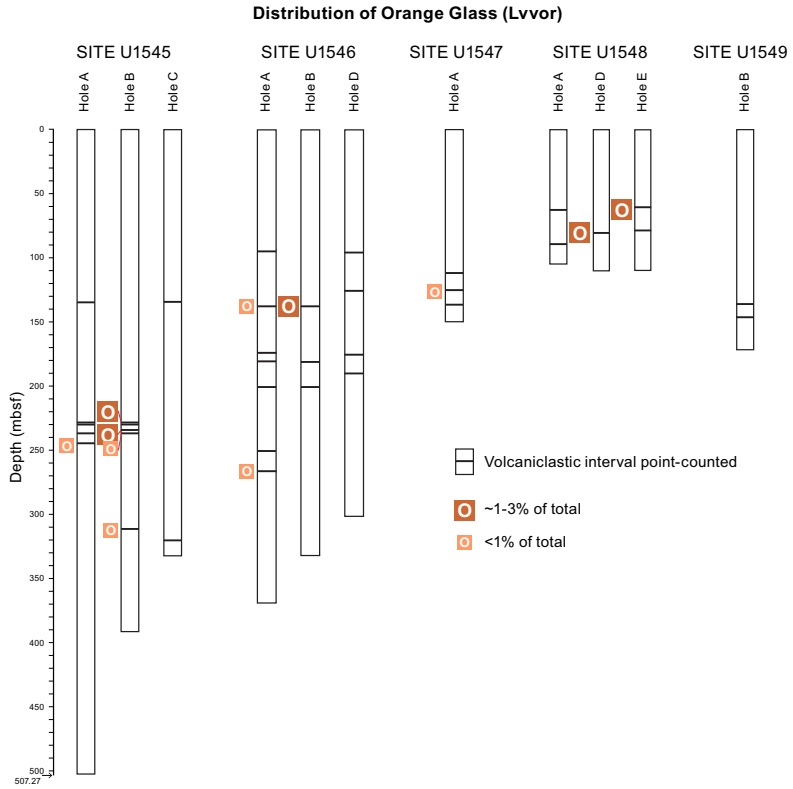

Figure F18. Total percent of orange glass (Lvvor) in samples from each site showing distribution of this component in site stratigraphy across basin, Sites U1545–U1549. Percentages taken from Table T6 based on data presented in Table T3.

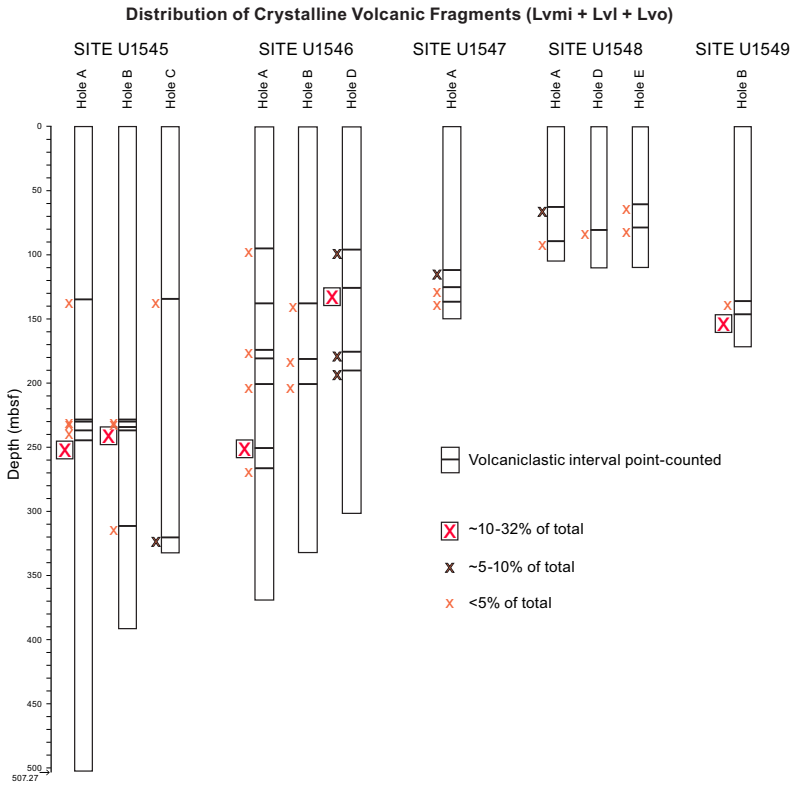

Figure F19. Total percent of crystalline volcanic fragments glass (Lvmi, Lvl, and Lvo) in samples from each site showing distribution of this component in site stratigraphy across basin, Sites U1545–U1549. Percentages taken from Table T6 based on data presented in Table T3.

U1545 and U1546, particularly notable at Site U1546 where the volcaniclastic intervals appear more broadly distributed downhole than at Site U1545 (Figure **F2**).

4. Closing remarks

In summary, macroscopic and petrographic analyses of volcaniclastic deposits reveal that various glass compositions with distinct morphologies are found in the Guaymas Basin, but the deposits are largely dominated by blocky light brown and altered glass. As demonstrated by Gadley and Marsaglia (2005) in their study of Cenozoic ash layers from Shatsky Rise during Ocean Drilling Program Leg 198, tephra correlation in deep ocean basins, such as the Guaymas Basin, cannot rely solely on compositional and textural data. Instead, it requires a combination of multiple techniques to constrain the source, timing, and spatial distribution of volcanic eruptions. In this data report, we do not discuss the origin of the fragments described herein or the reasons for their patterns of occurrence at individual sites and across the basin or attempt to correlate specific intervals. Such analysis will require additional geochemical data to be obtained from the volcanic particles.

5. Acknowledgments

We thank the Expedition 385 shipboard scientists for their meticulous and detailed work, which played an instrumental role in the development and execution of this project. The manuscript benefited from detailed reviews by Ryan Portner and Tobias W. Höfig.

This research used samples and data provided by the International Ocean Discovery Program (IODP). Funding for this project was provided by the National Science Foundation (Award OCE-2133396 to K. Marsaglia), U.S. Science Support Program for the International Ocean Discovery Program (Award 82A00CGG00939304 to K. Marsaglia and J. Stock), Geological Society of America (NSF/GSA Graduate Student Geoscience Grant to P. Martinez), and Society for Sedimentary Geology (SEPM Student Assistance Grant to P. Martinez).

References

Allen, R.W., 2021. Shedding new light on an enigmatic end member of back-arc spreading: the structure of the Grenada Basin in the Lesser Antilles. Journal of Geophysical Research: Solid Earth, 126(3):e2021JB021649. **https://doi.org/10.1029/2021JB021649**

Clague, D.A., Batiza, R., Head, J.W., III, and Davis, A.S., 2003. Pyroclastic and hydroclastic deposits on Loihi Seamount, Hawaii. In White, J.D.L., Smellie, J.L., and Clague, D.A. (Eds.), Explosive Subaqueous Volcanism. Geophysical Monograph, 140: 73–95. **https://doi.org/10.1029/140GM05**

Clague, D.A., Paduan, J.B., and Davis, A.S., 2009. Widespread strombolian eruptions of mid-ocean ridge basalt. Journal of Volcanology and Geothermal Research, 180(2–4):171–188. **https://doi.org/10.1016/j.jvolgeores.2008.08.007**

Critelli, S., and Ingersoll, R.V., 1995. Interpretation of neovolcanic versus palaeovolcanic sand grains: an example from Miocene deep-marine sandstone of the Topanga Group (Southern California). Sedimentology, 42(5):783–804. **https://doi.org/10.1111/j.1365-3091.1995.tb00409.x**

Critelli, S., Marsaglia, K.M., and Busby, C.J., 2002. Tectonic history of a Jurassic backarc-basin sequence (the Gran Cañon Formation, Cedros Island, Mexico), based on compositional modes of tuffaceous deposits. Geological Society of America Bulletin, 114(5):515–527. **https://doi.org/10.1130/0016-7606(2002)114<0515:THOAJB>2.0.CO;2**

Curray, J.R., Moore, D. G., et al., 1982. Initial Reports of the Deep Sea Drilling Project, 64: Washington, DC (US Government Printing Office). **https://doi.org/10.2973/dsdp.proc.64.1982**

Dickinson, W.R., 1970. Interpreting detrital modes of graywacke and arkose. Journal of Sedimentary Research, 40(2):695–707. **https://doi.org/10.1306/74D72018-2B21-11D7-8648000102C1865D**

Dürig, T., Schmidt, L.S., White, J.D.L., and Bowman, M.H., 2020a. DendroScan: an open source tool to conduct comparative statistical tests and dendrogrammatic analyses on particle morphometry. Scientific Reports, 10(1):21682. **https://doi.org/10.1038/s41598-020-78698-0**

Dürig, T., White, J.D.L., Zimanowski, B., Büttner, R., Murch, A., and Carey, R.J., 2020b. Deep-sea fragmentation style of Havre revealed by dendrogrammatic analyses of particle morphometry. Bulletin of Volcanology, 82(10):67. **https://doi.org/10.1007/s00445-020-01408-1**

Einsele, G., and Kelts, K., 1982. Pliocene and Quaternary mud turbidites in the Gulf of California; sedimentology, mass physical properties, and significance. In Curray, J.R., Moore, D. G., et al., Initial Reports of the Deep Sea Drilling

Project. 2, 64: Washington, DC (US Government Printing Office), 511–528. **https://doi.org/10.2973/dsdp.proc.64.107.1982**

Fisher, R.V., and Schmincke, H.-U., 1984. Pyroclastic Rocks: Berlin (Springer). **https://doi.org/10.1007/978-3-642-74864-6**

Gadley, K.L., and Marsaglia, K.M., 2005. Petrography and correlation of Cenozoic ash layers recovered on Shatsky Rise, ODP Leg 198. In Bralower, T.J., Premoli Silva, I., and Malone, M.J. (Eds.), Proceedings of the Ocean Drilling Program, Scientific Results. 198: College Station, TX (Ocean Drilling Program). **https://doi.org/10.2973/odp.proc.sr.198.108.2005**

Heiken, G., 1972. Morphology and petrography of volcanic ashes. Geological Society of America Bulletin, 83(7):1961–1988. **https://doi.org/10.1130/0016-7606(1972)83[1961:MAPOVA]2.0.CO;2**

Ingersoll, R.V., Bullard, T.F., Ford, R.L., Grimm, J.P., Pickle, J.D., and Sares, S.W., 1984. The effect of grain size on detrital modes: a test of the Gazzi-Dickinson point-counting method. Journal of Sedimentary Research, 54(1):103–116. **https://doi.org/10.1306/212F83B9-2B24-11D7-8648000102C1865D**

Marsaglia, K.M., 1991. Provenance of Sands and Sandstones from a Rifted Continental Arc, Gulf of California, Mexico. In Fisher, R.V., and Smith, G.A. (Eds.), Sedimentation in Volcanic Settings. SEPM Special Publication, 45. **https://doi.org/10.2110/pec.91.45.0237**

Marsaglia, K.M., 1992. Petrography and provenance of volcaniclastic sands recovered from the Izu-Bonin Arc, Leg 126. In Taylor, B., Fujioka, K., et al, Proceedings of the Ocean Drilling Program, Scientific Results. 126: College Station, TX (Ocean Drilling Program), 139–154. **https://doi.org/10.2973/odp.proc.sr.126.124.1992**

Marsaglia, K.M., 1993. Basaltic island sand provenance. In Johnsson, M.J., and Basu, A. (Eds.), Processes Controlling the Composition of Clastic Sediments. Geological Society of America Special Paper, 284: 41–66. **https://doi.org/10.1130/SPE284-p41**

Marsaglia, K.M., and Ingersoll, R.V., 1992. Compositional trends in arc-related, deep-marine sand and sandstone: a reassessment of magmatic-arc provenance. Geological Society of America Bulletin, 104(12):1637–1649. **https://doi.org/10.1130/0016-7606(1992)104<1637:CTIARD>2.3.CO;2**

Marsaglia, K.M., Mann, P., Hyatt, R.J., and Olson, H.C., 1999. Evaluating the influence of aseismic ridge subduction and accretion(?) on detrital modes of forearc sandstone: an example from the Kronotsky Peninsula in the Kamchatka Forearc. Lithos, 46(1):17–42. **https://doi.org/10.1016/S0024-4937(98)00054-1**

Martinez, P., 2022. Petrography and correlation of volcaniclastic intervals in the Quaternary marine sedimentary succession recovered during IODP Expedition 385 in Guaymas Basin, Gulf of California [MS thesis]. California State University. **http://hdl.handle.net/10211.3/224310**

Morrone, C., De Rosa, R., Le Pera, E., and Marsaglia, K.M., 2017. Provenance of volcaniclastic beach sand in a magmatic-arc setting: an example from Lipari island (Aeolian archipelago, Tyrrhenian Sea). Geological Magazine, 154(4):804–828. **https://doi.org/10.1017/S001675681600042X**

Morrone, C., Le Pera, E., De Rosa, R., and Marsaglia, K.M., 2018. Beach sands of Lipari island, Aeolian archipelago: roundness study. Rendiconti Online Societa Geologica Italiana, 45:141–146. **https://doi.org/10.3301/ROL.2018.42**

Morrone, C., Le Pera, E., Marsaglia, K.M., and De Rosa, R., 2020. Compositional and textural study of modern beach sands in the active volcanic area of the Campania region (southern Italy). Sedimentary Geology, 396:105567. **https://doi.org/10.1016/j.sedgeo.2019.105567**

Porritt, L.A., Russell, J.K., and Quane, S.L., 2012. Pele's tears and spheres: examples from Kilauea Iki. Earth and Planetary Science Letters, 333–334:171–180. **https://doi.org/10.1016/j.epsl.2012.03.031**

Portner, R.A., Clague, D.A., Helo, C., Dreyer, B.M., and Paduan, J.B., 2015. Contrasting styles of deep-marine pyroclastic eruptions revealed from Axial Seamount push core records. Earth and Planetary Science Letters, 423:219–231. **https://doi.org/10.1016/j.epsl.2015.03.043**

Powers, M.C., 1953. A new roundness scale for sedimentary particles. Journal of Sedimentary Research, 23(2):117–119. **https://doi.org/10.1306/D4269567-2B26-11D7-8648000102C1865D**

Rains, J.L., Marsaglia, K.M., and Dunne, G.C., 2012. Stratigraphic record of subduction initiation in the Permian metasedimentary succession of the El Paso Mountains, California. Lithosphere, 4(6):533–552. **https://doi.org/10.1130/L165.1**

Sarna-Wojcicki, A.M., Reheis, M.C., Pringle, M.S., Fleck, R.J., Burbank, D., Meyer, C.E., Slate, J.L., Wan, E., Budahn, J.R., Troxel, B., and Walker, J.P., 2005. Tephra layers of blind Spring Valley and related upper Pliocene and Pleistocene tephra layers, California, Nevada, and Utah: isotopic ages, correlation, and magnetostratigraphy. US Geological Survey Professional Paper, 1701. **https://doi.org/10.3133/pp1701**

Teske, A., Lizarralde, D., Höfig, T.W., Aiello, I.W., Ash, J.L., Bojanova, D.P., Buatier, M.D., Edgcomb, V.P., Galerne, C.Y., Gontharet, S., Heuer, V.B., Jiang, S., Kars, M.A.C., Khogenkumar Singh, S., Kim, J.-H., Koornneef, L.M.T., Marsaglia, K.M., Meyer, N.R., Morono, Y., Negrete-Aranda, R., Neumann, F., Pastor, L.C., Peña-Salinas, M.E., Pérez Cruz, L.L., Ran, L., Riboulleau, A., Sarao, J.A., Schubert, F., Stock, J.M., Toffin, L.M.A.A., Xie, W., Yamanaka, T., and Zhuang, G., 2021a. Expedition 385 summary. In Teske, A., Lizarralde, D., Höfig, T.W., and the Expedition 385 Scientists, Guaymas Basin Tectonics and Biosphere. Proceedings of the International Ocean Discovery Program, 385: College Station, TX (International Ocean Discovery Program). **https://doi.org/10.14379/iodp.proc.385.101.2021**

Teske, A., Lizarralde, D., Höfig, T.W., Aiello, I.W., Ash, J.L., Bojanova, D.P., Buatier, M.D., Edgcomb, V.P., Galerne, C.Y., Gontharet, S., Heuer, V.B., Jiang, S., Kars, M.A.C., Khogenkumar Singh, S., Kim, J.-H., Koornneef, L.M.T., Marsaglia, K.M., Meyer, N.R., Morono, Y., Negrete-Aranda, R., Neumann, F., Pastor, L.C., Peña-Salinas, M.E., Pérez Cruz, L.L., Ran, L., Riboulleau, A., Sarao, J.A., Schubert, F., Stock, J.M., Toffin, L.M.A.A., Xie, W., Yamanaka, T., and Zhuang, G., 2021b. Site U1546. In Teske, A., Lizarralde, D., Höfig, T.W., and the Expedition 385 Scientists,

Guaymas Basin Tectonics and Biosphere. Proceedings of the International Ocean Discovery Program, 385: College Station, TX (International Ocean Discovery Program). **https://doi.org/10.14379/iodp.proc.385.104.2021**

Waldman, R.J., Marsaglia, K.M., Hickey-Vargas, R., Ishizuka, O., Johnson, K.E., McCarthy, A., Yogodzinski, G., Samajpati, E., Li, H., Laxton, K., Savov, I.P., Meffre, S., Arculus, R.J., Bandini, A.N., Barth, A.P., Bogus, K., Brandl, P.A., Gurnis, M., and Jiang, F., 2020. Sedimentary and volcanic record of the nascent Izu-Bonin-Mariana arc from IODP Site U1438. Geological Society of America Bulletin, 133(7–8):1421–1440. **https://doi.org/10.1130/B35612.1**